AIAA JOURNAL
Vol. 41, No. 3, March 2003

Helmholtz-Like Resonator Self-Sustained Oscillations, Part 2: Detailed Flow Measurements and Numerical Simulations

S. Dequand*
Eindhoven University of Technology, 5600 MB Eindhoven, The Netherlands
S. Hulshoff†
Delft University of Technology, Kluyverweg 1, 2629 HS Delft, The Netherlands
and
H. van Kuijk,‡ J. Willems,§ and A. Hirschberg¶
Eindhoven University of Technology, 5600 MB Eindhoven, The Netherlands

A global description of the effect of the neck geometry on self-sustained oscillations of a grazing flow along a Helmholtz-like resonator has been given in a companion paper. Detailed flow measurements taken by means of hot-wire anemometry and numerical simulations based on the Euler equations for inviscid and two-dimensional compressible flows are now given. Vortex shedding is obtained in an inviscid flow simulation by considering a neck geometry with sharp edges at which the code predicts flow separation. Although two-dimensional flow calculations are attractive because of their computational efficiency, they are not able to represent the three-dimensional acoustical radiation from the resonator into free space without special frequency-dependent boundary condition treatments. Frequency-independent time-domain boundary conditions are considered. In view of the crudeness of this approximation, the agreement between theory and experiments is quite fair. The effects of changes in the geometry of the neck are qualitatively predicted by the model. The detailed flow information provides some insight into the influence of the shape of the upstream edge of the neck that could not be obtained from analytical models proposed in the companion paper.

Introduction

COUPLING between vortex shedding and acoustical resonance can induce self-sustained oscillations of the flow in a Helmholtz resonator and has been studied experimentally in the companion paper.[1] This phenomenon has been studied numerically, primarily using Navier–Stokes equations for two-dimensional compressible simulations (see Refs. 2–4). Hardin[5] also proposed a numerical method in which viscous flow is treated as a time-dependent incompressible flow. A combination of the incompressible blob method with an analogy has been considered by Peters[6] and Kriesels et al.[7] This incompressible flow approach is not suitable for describing feedback of the acoustical field on the flow, which is essential in our case.

We present numerical solutions for two-dimensional compressible flow computed using Euler equations. This reduces considerably the computational power required because we do not need to solve for the boundary-layer structure. The geometry considered is a deep cavity that consists of a volume and a neck, which, as explained in Ref. 1, we call a Helmholtz-like resonator.

Pulsation amplitude of the thick air jet flow grazing along the aperture of a Helmholtz-like resonator depends strongly on the geometry of the neck. A qualitative description of the phenomenon may be found in the companion paper,[1] which deals with analytical models and acoustical measurements. The present paper gives detailed information about the flow for a few neck geometries. Local velocity measurements made by means of a hot wire are compared to numerical predictions.

Four of the different configurations discussed in Ref. 1 have been chosen for this study. Configurations C_1–C_4 are shown in Fig. 1. The dimensions of the resonator are identical to those introduced in Ref. 1: the cavity is formed by a pipe with a square cross-sectional area $H^2 = 60 \times 60$ mm^2, the cavity length is $L = 191$ mm, and the neck width is $W = 26$ mm for configurations C_1 and C_3 and $W = 20$ mm for configurations C_2 and C_4. The neck opening has a cross-sectional area $H \times W$. The main flow is coming from left to right, and its velocity is U_0.

The acoustical velocity $\mathrm{d}\xi/\mathrm{d}t$ through the neck of the resonator can be deduced from acoustical pressure measurements.[1] As shown in Fig. 2, acoustical velocity amplitudes of the order of $0.5U_0$ are reached, in terms of Strouhal number $Sr = fW/U_0$, where f is the oscillation frequency, W is the width of the neck, and U_0 is the main velocity. The amplitudes measured for configurations C_1–C_3 are a factor of two larger than the acoustical velocity amplitude through the neck of the configuration C_4. We also observe a shift of the Strouhal number $Sr = fW/U_0$ at the maximum of amplitude from 0.25 for C_1–C_3 toward 0.33 for C_4. This confirms the important effect of both upstream and downstream edges. Analytical models, discussed in Ref. 1, do not provide an accurate prediction of such effects. In particular, they fail to explain the lack of difference between the behavior observed in configurations C_1 and C_3.

The outline of the remainder of the paper is as followed. In the next section, the experimental hot-wire measurements are described. Then, the numerical method is described, and its limitations are discussed. In the last section, numerical predictions are compared to experimental data and the effect of the neck geometry on the flow behavior is discussed.

Hot-Wire Velocity Measurements

General Description

The experimental setup used is described in Ref. 1. Hot-wire measurements provide a quantitative information about the absolute value $V = |\boldsymbol{V}|$ of the local flow velocity. In the resonator, the velocity vector $\boldsymbol{V}$ is the sum of the steady potential (irrotational) flow velocity $\boldsymbol{U}$, the local acoustical velocity $\boldsymbol{u}'$ (unsteady potential flow part of the velocity field), and the velocity $\boldsymbol{u}_{\mathrm{rot}}$ induced by vortices (rotational

Presented as Paper 2001-2228 at the AIAA/CEAS 7th Aeroacoustics Conference, Maastricht, The Netherlands, 28–30 May 2001; received 19 July 2001; revision received 18 October 2002; accepted for publication 21 October 2002.

*Postdoctoral Research Assistant, Faculty of Applied Physics, Postbus 513.
†Assistant Professor, Faculty of Aerospace Engineering, Kluyverveg 1.
‡Student, Faculty of Applied Physics, Postbus 513.
§Senior Engineer, Faculty of Applied Physics, Postbus 513.
¶Professor, Faculty of Applied Physics, Postbus 513.

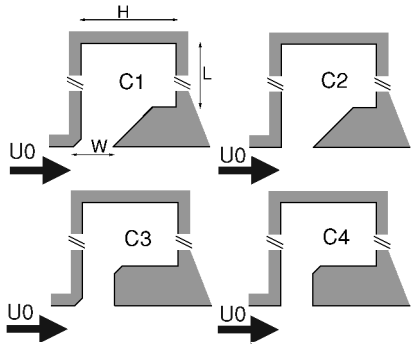

Fig. 1 Configurations studied.

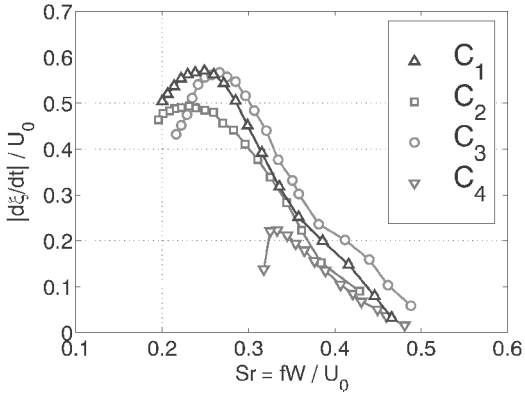

Fig. 2 Dimensionless acoustical velocity amplitude $|d\xi/dt|/U_0$ in terms of the Strouhal number $Sr = fW/U_0$ in the neck: △, configuration C_1; □, configuration C_2; ○, configuration C_3; and ▽, configuration C_4.

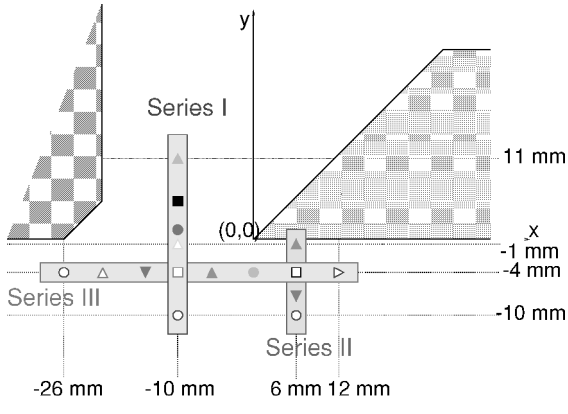

Fig. 3 Hot-wire locations in the measurements: symbols used represent measured and predicted velocity magnitudes.

part of the velocity field):

$$\boldsymbol{V} = \boldsymbol{U} + \boldsymbol{u}' + \boldsymbol{u}_{\text{rot}} \tag{1}$$

A Dantec (Type 55P11) hot-wire anemometer was used in combination with the software Streamline and the hardware Streamware from Dantec as the acquisition system.

The hot wire was made of a platina wire with a diameter of 5 μm and a length of 5 mm.

Hot-Wire Positions

The position of the hot wire could be varied in the x and y directions in the main flow direction and normal to the flow, respectively. The position was measured within an accuracy of about 0.1 mm.

Figure 3 shows the different locations for which velocity measurements were performed and introduces the symbols used to denote the position for the values appearing subsequently. The origin of the frame of reference was chosen at the downstream edge of the neck. For series I, the hot-wire position was varied in the y direction from -10 to 11 mm while being held fixed in the x direction at $x = -10$ mm. For series II, the hot-wire location was varied in the y direction from -10 to -1 mm while being held fixed in the x direction at $x = 6$ mm. Series III was a horizontal sweep, where the hot-wire position was held fixed at $y = -4$ mm while the x position was varied from $x = -26$ to $x = 12$ mm.

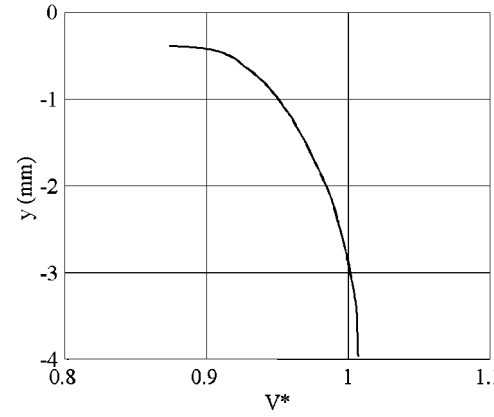

Fig. 4 Boundary-layer profile upstream of the neck opening (at $x = -32$ mm in the reference frame given in Fig. 3).

Upstream Boundary-Layer Profile

Figure 4 shows the ratio $V^* = V/U_0$ of the velocity magnitude V and the main flow velocity U_0 measured just upstream of the neck opening for different locations of the hot-wire in the y direction. This gives information about the boundary-layer profile upstream of the neck of the resonator. We see that the boundary-layer displacement thickness is about 0.5 mm.

The distance between the settling chamber convergence and the upstream edge of the mouth of the resonator is $\ell = 115$ mm. This corresponds, for typical flow velocities of $U_0 = 30$ m/s, with a Reynolds number $Re_\ell = U_0\ell/\nu = 2.3 \times 10^5$ so that we expect a turbulent or a transitional boundary layer. By placing a strip of sand paper on the pipe wall just upstream of the mouth opening of the resonator, we forced turbulence.[8]

Numerical Simulations

Approach

For the numerical simulations, we used a two-dimensional Euler method for inviscid compressible flows.[9] The spatial discretization method was based on a second-order cell-centered finite volume method. A four-stage Runge–Kutta method was used for time integration. The code was tuned to allow for accurate prediction of acoustic wave propagation and was verified on several acoustical test problems.[9,10]

Numerical Domain

The numerical domain was made up of structured grid blocks. Two resonator widths away from the neck, within the cavity of the resonator (inner domain) and outside the resonator (outer domain) at the downstream side, the domain was built up of blocks with a gradually decreasing number of cells. This allowed an accurate description of the near field and avoided excessive refinement of the low-frequency plane-wave propagation region.

Initial Condition

Computations were started by specifying a pressure profile, corresponding to an harmonic standing wave at the phase corresponding to a zero velocity in the resonator as an initial condition. The initial acoustical pressure amplitude at the top of the resonator was chosen equal to the amplitude of the measured acoustic pressure p'_{exp} at the end wall of the cavity.

Boundary Conditions

In the numerical algorithm, boundary conditions are applied by specifying the state of halo cells (surrounding the numerical

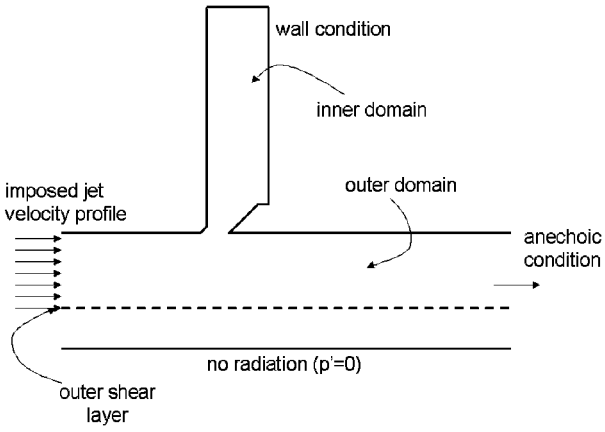

Fig. 5 Numerical domain and scheme of the boundary conditions imposed.

domain). This is done by means of a local discretization of the compatibility relations, similar to that of Thompson[11,12] and Poinsot and Lele.[13]

Figure 5 shows a scheme of the boundary conditions imposed on the numerical domain. Solid-wall conditions were used to define the cavity and adjacent walls, whereas an anechoic boundary condition was applied at the outflow. Application of an appropriate condition for the lower outer boundary proved to be more difficult. A major limitation of two-dimensional computations with frequency-independent time-domain boundary conditions is their inability to account properly for the three-dimensional free-field radiation[14] present in the experiments. The three-dimensional radiation at such low frequencies is very low, suggesting the use of $p' = 0$ as boundary condition. Numerical experiments showed that the best results are indeed obtained by imposing a zero acoustic pressure ($p' = 0$) condition on the lower outer boundary.

The remaining inflow boundary (Fig. 5) was treated using a "soft" constant-velocity condition. On the lower part of the boundary, a zero velocity was specified, whereas on the upper part the experimental value of the jet inflow velocity U_0 was specified. For all cases, the grazing jet had a width H of 60 mm as in the experiments at the exit of the wind tunnel.[1]

The soft constant-velocity condition was applied by specifying the strength of incoming acoustic waves to be directly proportional to the difference between the instantaneous velocity and the desired velocity, multiplied by a relaxation factor. For our calculations, this factor was fixed at a value of 0.5. This combination maintained the desired velocity for low-frequency disturbances, but allowed temporary deviations from the desired value for high-frequency disturbances. Therefore this condition functioned as a rough model for the truncated upstream portion of the domain. Note that it is also possible to specify a constant-velocity condition directly using the compatibility relations. This type of hard condition will maintain the desired velocity at all times, and, therefore, directly reflect upstream-traveling acoustic waves. For the current study, this boundary condition introduces a strong dependence of the acoustic pressure amplitude in the resonator on the upstream length of the outer domain.

The performance of the soft condition was investigated for several upstream lengths of the outer domain. It was found that above a critical length (half of the resonator width H), the predicted amplitude of the acoustical pressure in the resonator converged toward a mean value independent of the length of the upstream block. There was, however, some amplitude modulation of the pressure signal, which varied with the length of the upstream outer domain. This is discussed further in another subsection.

Kutta Condition

The numerical method makes use of an added artificial viscosity term to ensure nonlinear stability. Although the magnitude of this dissipation is grid dependent (decreasing with grid refinement), it is always of appreciable magnitude near a sharp edge due to high local cell-to-cell gradients. This is usually sufficient to ensure separation and to enforce the Kutta condition (see Ref. 15). Numerical separation is often accompanied by the creation of a shear layer, however, whose thickness and therefore stability will be grid dependent. To avoid this grid dependence, extra diffusion terms can be added to the Euler equations before discretization. The net effect is to eliminate the grid dependence of the shear layer thickness within the numerical domain.

Refinement and Domain Size

The dependence of the numerical results on grid refinement was investigated by comparing fine-, intermediate-, and coarse-grid results. The fine grid had twice the refinement of the intermediate grid and four times the refinement of the coarse grid in both x and y directions. In the neck region, the intermediate grid had 30×45 cells. In general, the refinement of the intermediate grid was found sufficient to provide a satisfactory level of grid independence. Artificial dissipation needed to maintain numerical stability decreases rapidly with the grid refinement [$\mathcal{O}(\Delta x^2)$]. To preserve numerical stability, a diffusive term was added to the Euler equations. The magnitude of the diffusive term in the momentum equations was matched to be of the order of magnitude of molecular viscous terms. A study of the effect of the artificial dissipation and diffusion parameters on the numerical results has been performed. Although details of the flow are affected by changes in those parameters, the predicted pulsation amplitude remained constant within 10% when the model did predict oscillations.

The influence of the length of the upstream outer domain on the numerical results was also investigated. A dependence of the amplitude modulation of the acoustic pressure on this upstream domain length was observed. This amplitude modulation was the result of an instability in the outer shear layer separating the jet from the region where a zero flow velocity was initially imposed (Fig. 6). The oscillation of the outer shear layer has been observed by flow visualization in a study of the effect of the jet thickness on the pulsation amplitudes.[16] The period doubling is, however, not observed experimentally. We expect that this effect is exaggerated in our two-dimensional simulations of the outer domain compared to the actual three-dimensional flow in the freejet.

Computed Results

Numerical simulations have been performed for configurations C_1–C_4 (Fig. 1). All of the numerical results shown in the next sections have been obtained using the fine mesh with an upstream block length twice the resonator width. This corresponds to the position of the outlet of the wind tunnel in the experiments. Numerical probes are placed at the same location as the hot wire (Fig. 3), and the total velocity is calculated from the computed components of the velocity $\boldsymbol{v} = (v_x, v_y)$:

$$V^*_{\text{num}} = \sqrt{v_x^2 + v_y^2}/U_0 \tag{2}$$

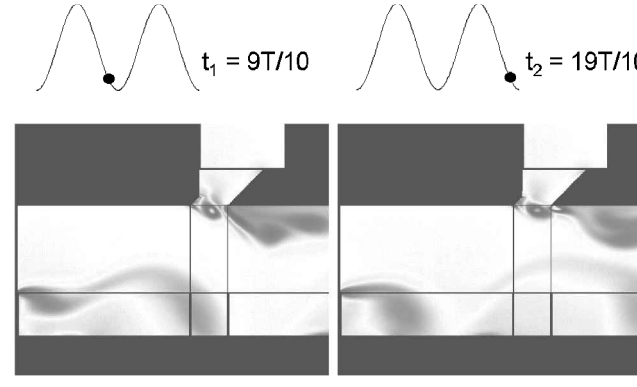

Fig. 6 Configuration C_1, predicted vorticity magnitude when soft inflow condition is used; comparison between two consecutive acoustic oscillation periods. Note that flow is not exactly periodic and there is period doubling.

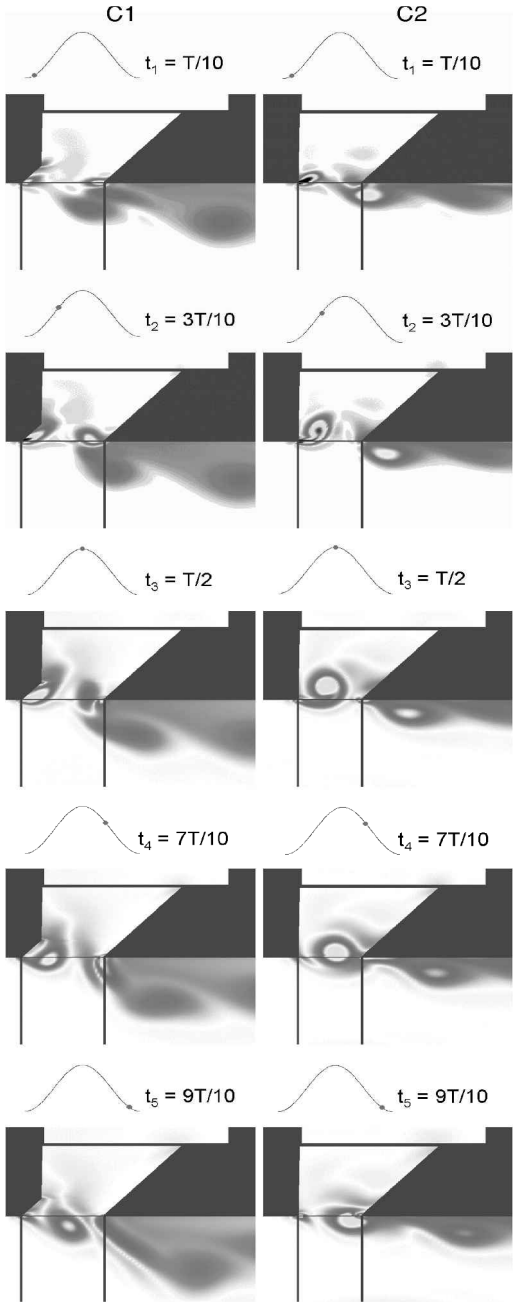

Fig. 7 Vorticity magnitude in the neck of configurations C_1 ($Sr = 0.285$) and C_2 ($Sr = 0.284$) with the corresponding time on the acoustical pressure signal.

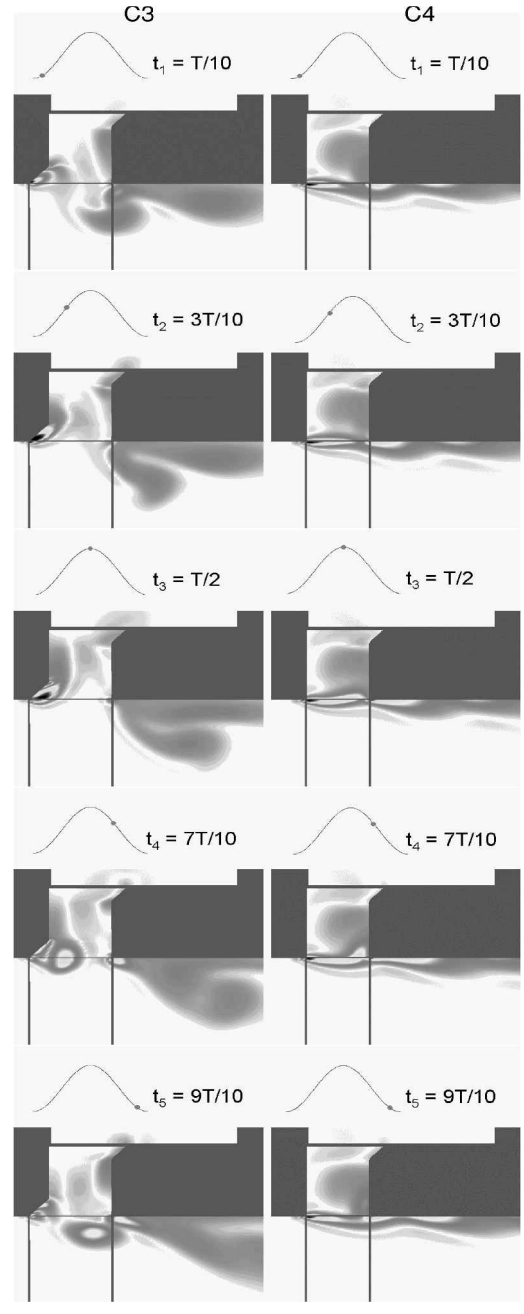

Fig. 8 Vorticity magnitude in the neck of configurations C_3 ($Sr = 0.26$) and C_4 ($Sr = 0.35$) with the corresponding time on the acoustical pressure signal.

Figures 7 and 8 show the periodic vortex shedding in the neck of the resonator that was typically observed after a steady oscillation was well established. In practice, we calculated up to 30 periods after the initial transient behavior. A steady state was already approached after 10 oscillation periods. Figures 7 and 8 show the vorticity magnitude distribution predicted for configurations C_1–C_4 at different times within one period of oscillation. The corresponding dimensionless time t/T on the acoustical pressure signal is also shown.

In Fig. 9, we compare the vortex path in the neck of the resonator for the four different configurations, C_1–C_4. The center of the vortex is determined visually from the vorticity magnitude predicted by the Euler computations (Figs. 7 and 8). This was done during two consecutive periods. The filled symbols represent the center of the vortex during the first period whereas the open symbols correspond to the location of the vortex during the second period.

We see that the vortex path of configurations with a chamfered upstream edge (C_1 and C_3) are very close to each other near the upstream edge (Figs. 7 and 8), but the vortex seems to travel faster through the neck of configuration C_3. In configuration C_2 (with a

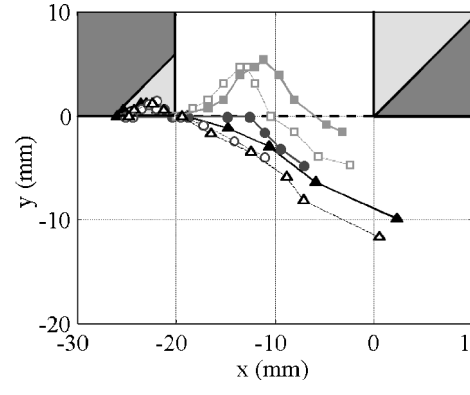

Fig. 9 Location of vortex center in neck; first and second period of acoustical oscillations: ○, configuration C_1 second period; ●, configuration C_1 first period; □, configuration C_2 second period; ■, configuration C_2 first period; △, configuration C_3 second period; ▲, configuration C_3 first period; and – – –, configuration C_4.

sharp upstream edge, Fig. 7), the vortex enters more deeply into the neck than for the other configurations, before it is ejected out of the neck. For configuration C_4, isolated vortex structures are not clearly observed. It is difficult to determine the vortex path. We assume it to be very close to the straight line joining the upstream to the downstream edge of the neck. This is similar to the low-amplitude flow visualization reported by Bruggeman[17] and Peters[6] for closed-side branch resonators.

For a chamfered upstream edge (configurations C_1 and C_3), the pressure fluctuation amplitude is rather insensitive to the shape of the downstream edge.[1] This observation could be explained by the fact that, for a chamfered upstream edge, the vortex path remains far from the downstream edge. For a sharp upstream edge (configurations C_2 and C_4), we note that there is a strong interaction of the vortex with the downstream edge. Consequently, the measured acoustical amplitudes do depend on the shape of this edge. This effect of the upstream edge on the path of the vortex has been confirmed by flow visualization.

Results of Local Velocity Measurements

Comparison Between Experimental and Numerical Results: Raw Data

Figure 10 presents the time dependence of the dimensionless acoustical pressure $p^* = p'/p'_{\text{exp}}$ at the top of the resonator cavity ($y = L$) of configuration C_3. In Fig. 10a, the measured pressure signal is almost perfectly periodic, whereas the computed pressure signal (Fig. 10b) shows a modulation in amplitude. This modulation is due to the instability of the outer shear layer that occurs in the computations.

We see also that the mean numerical pressure is not equal to the atmospheric pressure (Fig. 10). This overpressure could not be measured by means of the piezoelectrical pressure transducers, which do not measure such a continuous component of the pressure signal. The mean static pressure $\langle p \rangle$ was measured separately by means of a piezoresistive gauge (Kulite Type XCS-093-2G) placed at the top of the resonator. The result of those measurements is shown in Fig. 11 as a function of the Strouhal number $Sr = fW/U_0$. The typical measured dimensionless pressure $\langle p \rangle / \frac{1}{2}\rho_0 U_0^2$ (where ρ_0 is the density of air) is about a factor of two lower than the predicted value (filled symbols). Such a difference can be due to the lack of turbulence in the numerical model, which affects the entrainment of air outside of the cavity by the shear layer. This difference could induce a systematic deviation between the predicted and the actual vortex path. This problem deserves further research. We observe that the measured pressure $\langle p \rangle$ depends strongly on the geometry of the upstream edge of the neck. The Euler calculations also predict such an effect, but it is less pronounced.

The Euler computations predict the resonance frequency within 5%. The two-dimensional description of the outer flow exaggerates its acoustical inertia. This results into a systematic error in the predicted frequency that is lower than the measured oscillation frequency. Figure 12 shows the predicted pulsation amplitudes $|\mathrm{d}\xi/\mathrm{d}t|/U_0$ in terms of the Strouhal number $Sr = fW/U_0$. Numerical predictions are denoted by the filled symbols. The amplitude of the acoustical velocity is deduced from the predicted amplitude of the pressure oscillation in the cavity. The experimental results are represented with corresponding open symbols in Fig. 12. We see that the Euler method underestimates the maximum of the pulsation amplitudes by about 20% for configurations C_1–C_3. At higher Strouhal number, the prediction is globally too low by a factor of two for configurations C_1–C_3. The predicted amplitude for configuration C_4 is too low by about a factor of four.

Figure 13 presents typical raw data obtained for the velocity signals (configuration C_3). The numerical velocity signal is much smoother than the measured signal because the two-dimensional Euler equations do not include the effects of turbulence. Although experimental and numerical results are different, we can observe some similarities.

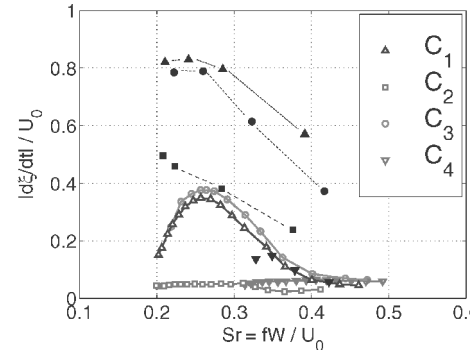

Fig. 11 Dimensionless mean static pressure $\langle p \rangle / \frac{1}{2}\rho_0 U_0^2$ in neck of configurations C_1–C_4 in terms of Strouhal number $Sr = fW/U_0$: comparison between experimental (open symbols) and numerical (filled symbols) results.

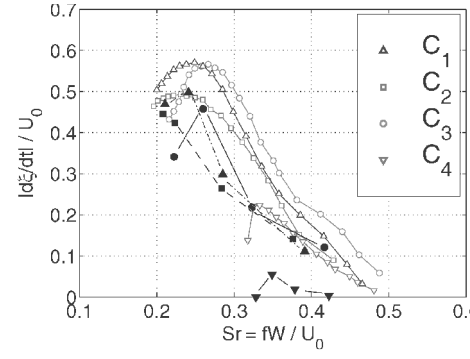

Fig. 12 Dimensionless acoustical velocity amplitude $|\mathrm{d}\xi/\mathrm{d}t|/U_0$ in neck of configurations C_1–C_4 in terms of Strouhal number $Sr = fW/U_0$: comparison between experimental (open symbols) and numerical (filled symbols) results.

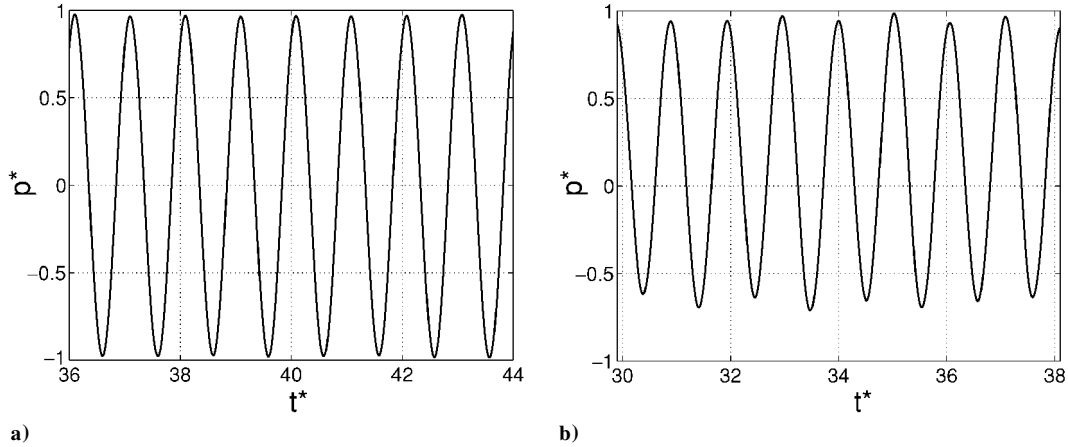

Fig. 10 Time dependence of dimensionless acoustical pressure $p^*(t) = p'(t)/p'_{\text{exp}}$ at the top of the resonator (configuration C_3, $Sr \approx 0.27$); comparison between a) experimental and b) numerical results.

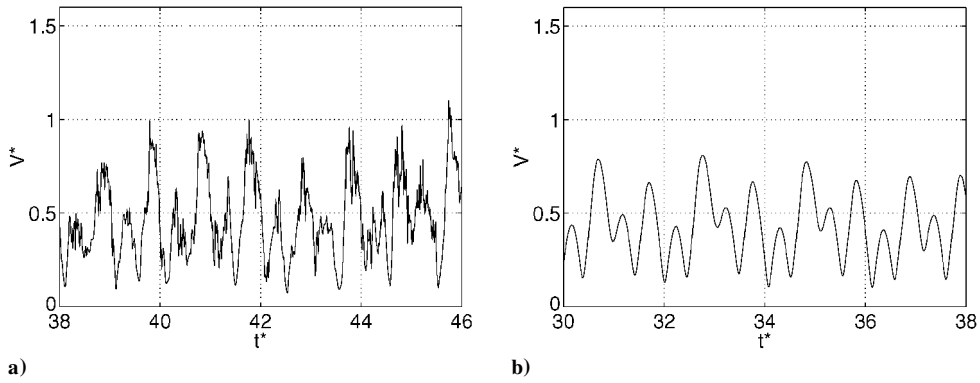

Fig. 13 Time dependence of the dimensionless velocity $V^*(t) = V/U_0$ in neck of configuration C_3 ($Sr \approx 0.27$) where $x = -10$ mm, and $y = 1$ mm; see Fig. 3. Comparison between a) experimental and b) numerical results.

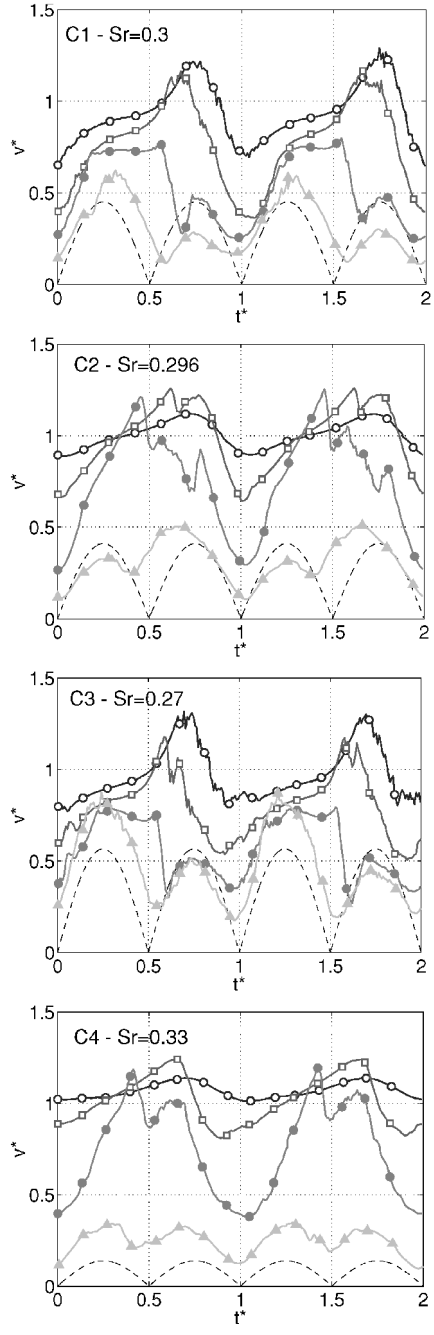

Fig. 14 Experimental results for series I, where measured acoustical velocity amplitudes are $(|d\xi/dt|/U_0)_{C_1} = 0.4507$, $(|d\xi/dt|/U_0)_{C_2} = 0.4107$, $(|d\xi/dt|/U_0)_{C_3} = 0.5666$, and $(|d\xi/dt|/U_0)_{C_4} = 0.1380$: symbols as defined in Fig. 3, and – – –, acoustical velocity amplitude as reference.

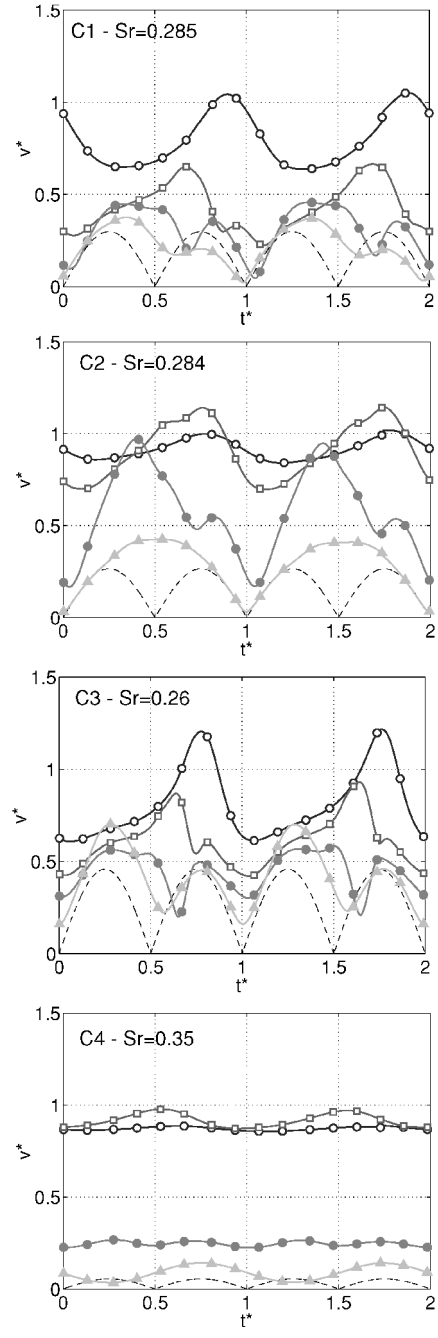

Fig. 15 Numerical results for series I, where predicted acoustical velocity amplitudes are $(|d\xi/dt|/U_0)_{C_1} = 0.2986$, $(|d\xi/dt|/U_0)_{C_2} = 0.2650$, $(|d\xi/dt|/U_0)_{C_3} = 0.4576$, and $(|d\xi/dt|/U_0)_{C_4} = 0.0552$: symbols as defined in Fig. 3, and – – –, acoustical velocity amplitude as reference.

Comparison Between Experimental and Numerical Results: Averaged Signals

Instead of considering the original hot-wire data, we will focus on phase-averaged signals. The averaging is based on a periodicity of twice the period of the pressure signal, which is our reference. This will allow to see the period doubling but will somewhat smooth out the data. As time origin, we choose the moment at which the acoustical pressure in the resonator is minimal. That is when the acoustical velocity starts entering in the resonator. In our analytical model described in Ref. 1, this corresponds to the moment at which a vortex is shed at the upstream edge of the neck. Note that this seems in agreement with our numerical simulations (Figs. 7 and 8). The phase averaging is made on a given number of oscillation periods. To preserve high-frequency components of the oscillations, we have limited the number of oscillation periods used for the averaging to 20.

In Figs. 14–17, results are presented in a dimensionless form. The time dependence of the absolute value of the acoustical velocity $|d\xi/dt|$ in the neck of the resonator is plotted (dashed line) as a reference in each graph. For each measurements series (notations and symbols introduced in Fig. 3) and for each configuration, experimental results are compared to numerical results.

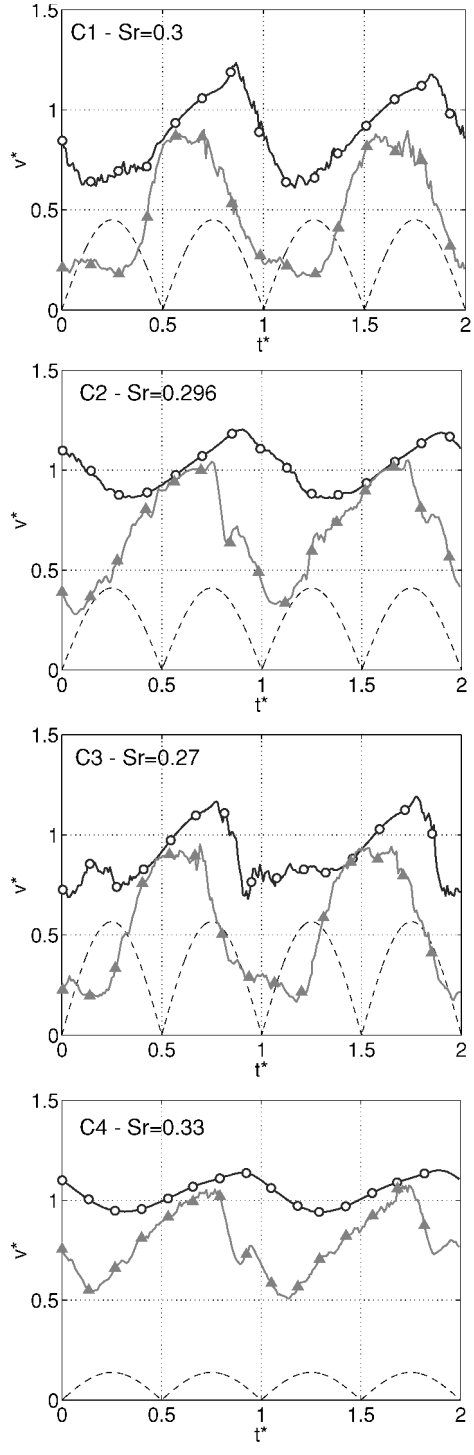

Fig. 16 Experimental results for series II, where measured acoustical velocity amplitudes are $(|d\xi/dt|/U_0)_{C_1} = 0.4507$, $(|d\xi/dt|/U_0)_{C_2} = 0.4107$, $(|d\xi/dt|/U_0)_{C_3} = 0.5666$, and $(|d\xi/dt|/U_0)_{C_4} = 0.1380$: symbols as defined in Fig. 3, and – – –, acoustical velocity amplitude as reference.

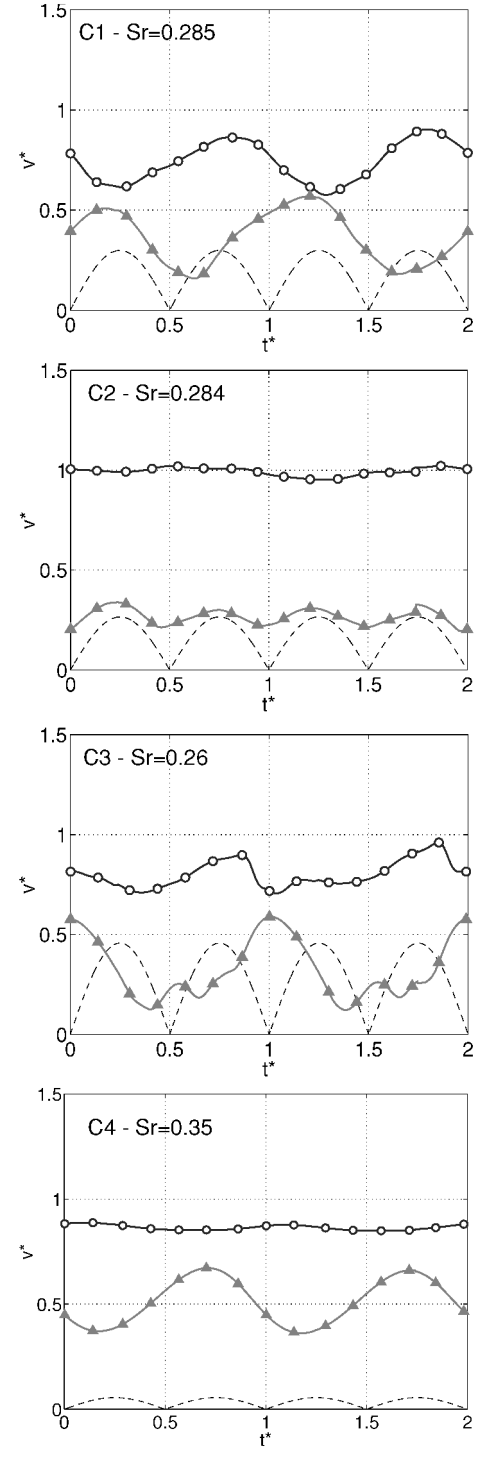

Fig. 17 Numerical results for series II, where predicted acoustical velocity amplitudes are $(|d\xi/dt|/U_0)_{C_1} = 0.2986$, $(|d\xi/dt|/U_0)_{C_2} = 0.2650$, $(|d\xi/dt|/U_0)_{C_3} = 0.4576$, and $(|d\xi/dt|/U_0)_{C_4} = 0.0552$: symbols as defined in Fig. 3, and – – –, acoustical velocity amplitude as reference.

For measurement series I (Fig. 14), the velocity amplitude $V^* = V/U_0$ has two different typical behaviors. For points deep in the neck (filled symbols), the mean flow velocity is zero, and the total velocity amplitude depends mainly on the acoustical velocity (dashed line). This explains the rather low amplitudes observed compared to the velocity amplitude measured when the points are outside of the neck (open symbols). For these points, we observe the passage of a vortex. The incursion of the vortex into the neck is clearly seen for configuration C_2 (Fig. 14, filled circle). This indeed corresponds to the numerical prediction of the vortex path (Fig. 9). For configuration C_4, the acoustic amplitude is relatively low but the velocity behavior is surprisingly similar to that observed in configuration C_2.

Figure 15 presents the averaged velocity amplitude predicted by the Euler calculations for series I. The predicted response is globally fair but with a smaller amplitude than the measured velocity amplitude. For the particular points considered, the amplitudes predicted for configuration C_3 are 20% too low. For configurations C_1 and C_2, they are 40% too low. For configuration C_4, the numerical calculations were performed at a Strouhal number $Sr \approx 0.35$ because computations performed at $Sr \approx 0.32$ did not display any self-sustained oscillations of the flow. At Strouhal $Sr \approx 0.35$, the predicted pressure amplitude was still too low by a factor of four (Fig. 12). This explains the dramatic difference between the measured and predicted averaged velocity signals for configuration C_4 (Figs. 14 and 15).

For measurement series II (Fig. 16), we focus on the flow behavior just downstream of the downstream edge. The relatively low total velocity amplitude observed when the hot wire is located very close to the wall (1 mm from the wall, filled trangle) is expected to be due to the presence of the viscous wall-boundary layer, which is not included in Euler calculations. Once again, the total velocity signals for configurations C_1 and C_3 are very similar. Some similarity is also found between the flow behavior in configurations C_2 and C_4.

Numerical results for series II (Fig. 17) differ substantially from experimental results. Except for configuration C_3, the vortex shedding at the downstream edge is not well predicted. We see a much smoother velocity profile than the measured one.

The results of series III confirm the results of series I and II.[8]

Conclusions

Four different neck geometries C_1–C_4 have been considered. Numerical simulations and hot-wire velocity measurements have been performed. The measurement of the velocity in the neck of the different configurations gives global information about the flow behavior in the neck of the resonators. This is confirmed by the predicted vorticity magnitude, which gives an overview of the vortex shedding in the neck of resonators. A parallel can be drawn between the experimental flow behavior in configurations C_1 and C_3 with a chamfered upstream edge (Fig. 1). In the same way, the results obtained for configurations C_2 and C_4, with a sharp upstream edge, are similar. This means that the flow behavior depends strongly on the geometry of the upstream edge (rounded or sharp). The downstream-edge geometry determines the oscillation amplitude when the upstream edge is sharp but seems to affect the flow behavior less. This can be observed by comparison of the velocity measured in configuration C_4 with that measured in configuration C_2. For a chamfered upstream edge (configurations C_1 and C_3), our numerical simulations show that the vortex path remains remote from the downstream edge (Fig. 9). This has been confirmed by flow visualization. This could partially explain why the pulsation amplitude in this case is insensitive to the shape of the downstream edge.[1] For a sharp upstream edge, the vortex path enters into the neck and passes close to the downstream edge.

Euler computations predict within 20% the maximum of the amplitude of the acoustical pressure for the configurations C_1–C_4. The Strouhal number dependence of the pulsation amplitude is quite well predicted. The results are less satisfactory for configuration C_4. The amplitude is underestimated by about a factor of four. Numerical simulations do, however, predict the significant lowering of the amplitude in the case of configuration C_4, compared to the cases of configurations C_1–C_3.

The agreement between the experimental and numerical velocity profiles depends on the quality of the prediction of the pulsation amplitude. This is much better for the Strouhal number condition chosen for configuration C_3, than for the other configurations. Furthermore, the flow downstream of the neck is not predicted as well as the flow within the neck opening.

We observe a difference between the measured and the calculated mean static pressure in the resonators. This deserves further research to evaluate the impact of this pressure difference on the vortex path and, hence, on the sound production. Furthermore, this static pressure data could be used to test the performance of turbulent flow models.

Acknowledgments

This work has been carried out within the framework of the European Project "Flow Duct Acoustics" (FLODAC, BRPR CT97-10394). We thank Lionel Hirschberg and Robbie Balk for performing flow visualization.

References

[1]Dequand, S., Luo, X., Willems, J., and Hirschberg, A., "Helmholtz-Like Resonator Self-Sustained Oscillations, Part 1: Acoustical Measurements and Analytical Models," *AIAA Journal*, Vol. 41, No. 3, 2003, pp. 408–415.

[2]Rowley, C. W., Colonius, T., and Basu, A. J., "On Self-Sustained Oscillations in 2D Compressible Flow over Rectangular Cavities," *Journal of Fluid Mechanics*, Vol. 455, March 2002, pp. 315–346.

[3]Gloerfelt, X., Bailly, C., and Juvé, D., "Simulation Numérique du Bruit Rayonné par une Cavité Excitée par un Écoulement," *Proceedings of the 5th French Congress on Acoustics*, Presses Polytechniques et Universitaires Romandes, Lausanne, Switzerland, 2000, pp. 554–557.

[4]Ricot, D., Maillard, V., and Bailly, C., "Numerical Simulation of the Unsteady Flow past a Cavity and Application to the Sunroof Buffeting," AIAA Paper 2001-2112, May 2001.

[5]Hardin, J. C., and Pope, D. S., "Sound Generation by Flow over a Two-Dimensional Cavity," *AIAA Journal*, Vol. 33, No. 3, 1995, pp. 407–412.

[6]Peters, M. C. A. M., "Aeroacoustic Sources in Internal Flows," Ph.D. Dissertation, Faculty of Applied Physics, Eindhoven Univ. of Technology, Eindhoven, The Netherlands, Sept. 1993.

[7]Kriesels, P. C., Peters, M. C. A. M., Hirschberg, A., Wijnands, A. P. J., Iafrati, A., Riccardi, G., Piva, R., and Bruggeman, J. C., "High Amplitude Vortex-Induced Pulsations in a Gas Transport System," *Journal of Sound and Vibration*, Vol. 184, No. 2, 1995, pp. 343–368.

[8]Dequand, S., "Duct Aeroacoustics: From Technological Applications to the Flute," Ph.D. Dissertation, Faculty of Applied Physics, Eindhoven Univ. of Technology, Eindhoven, The Netherlands, and Univ. du Maine, Le Mans, France, Dec. 2001.

[9]Hulshoff, S. J., "EIA: an Euler Code for Internal Aeroacoustics, Part 1: Method Description and User's Guide," TR R-1545-D, Eindhoven Univ. of Technology, Eindhoven, The Netherlands, April 2001.

[10]Dequand, S., "EIA: an Euler Code for Internal Aeroacoustics, Part 2: Example Computations," TR R-1545-D, Eindhoven Univ. of Technology, Eindhoven, The Netherlands, April 2001.

[11]Thompson, K. W., "Time-Dependent Boundary Conditions for Hyperbolic Systems," *Journal of Computational Physics*, Vol. 68, No. 1, 1987, pp. 1–24.

[12]Thompson, K. W., "Time-Dependent Boundary Conditions for Hyperbolic Systems II," *Journal of Computational Physics*, Vol. 89, No. 2, 1990, pp. 439–461.

[13]Poinsot, T. J., and Lele, S. K., "Boundary Conditions for the Direct Simulation of Compressible Viscous Flows," *Journal of Computational Physics*, Vol. 101, No. 1, 1992, pp. 104–129.

[14]Pierce, A. D., *Acoustics: an Introduction to Its Physical Principles and Applications*, Acoustical Society of America, 1989.

[15]Hirsch, C., *Numerical Computation of Internal and External Flow*, Vol. 2, Series in Numerical Methods, Wiley-Interscience, Chichester, England, U.K., 1990.

[16]Dequand, S., Willems, J. F. H., Leroux, M., Vullings, R., van Weert, M., Thieulot, C., and Hirschberg, A., "Simplified Models of Flue Instruments: Effect of Pipe Acoustics and of Mouth Geometry," *Journal of the Acoustical Society of America* (to be published).

[17]Bruggeman, J. C., "Flow Induced Pulsations in Pipe Systems," Ph.D. Dissertation, Faculty of Applied Physics, Eindhoven Univ. of Technology, Eindhoven, The Netherlands, June 1987.

P. J. Morris
Associate Editor